

# Evidence for the Band-Edge Exciton of CuInS<sub>2</sub> Nanocrystals Enables Record Efficient Large-Area Luminescent Solar Concentrators

Abhinav Anand, Matteo L. Zaffalon, Graziella Gariano, Andrea Camellini, Marina Gandini, Rosaria Brescia, Chiara Capitani, Francesco Bruni, Valerio Pinchetti, Margherita Zavelani-Rossi, Francesco Meinardi,\* Scott A. Crooker, and Sergio Brovelli\*

Ternary I-III-VI<sub>2</sub> nanocrystals (NCs), such as CuInS<sub>2</sub>, are receiving attention as heavy-metals-free materials for solar cells, luminescent solar concentrators (LSCs), LEDs, and bio-imaging. The origin of the optical properties of CuInS<sub>2</sub> NCs are however not fully understood. A recent theoretical model suggests that their characteristic Stokes-shifted and long-lived luminescence arises from the structure of the valence band (VB) and predicts distinctive optical behaviours in defect-free NCs: the quadratic dependence of the radiative decay rate and the Stokes shift on the NC radius. If confirmed, this would have crucial implications for LSCs as the solar spectral coverage ensured by low-bandgap NCs would be accompanied by increased re-absorption losses. Here, by studying stoichiometric CuInS<sub>2</sub> NCs, it is revealed for the first time the spectroscopic signatures predicted for the free band-edge exciton, thus supporting the VB-structure model. At very low temperatures, the NCs also show dark-state emission likely originating from enhanced electron-hole spin interaction. The impact of the observed optical behaviours on LSCs is evaluated by Monte Carlo ray-tracing simulations. Based on the emerging device design guidelines, optical-grade large-area (30×30 cm<sup>2</sup>) LSCs with optical power efficiency (OPE) as high as 6.8% are fabricated, corresponding to the highest value reported to date for large-area devices.

technologies including photovoltaic (PV) cells,<sup>[1]</sup> luminescent solar concentrators (LSCs),<sup>[2]</sup> light emitting diodes,<sup>[3]</sup> as well as bioimaging<sup>[3d,4]</sup> where their inherent lower toxicity offers a significant advantage over Cd- and Pb-based NCs. In addition to their heavy-metal-free composition, I-III-VI<sub>2</sub> NCs feature important electronic and photophysical properties, such as degenerate p-type transport<sup>[5]</sup> and broadband absorption tunable from visible to near infrared<sup>[6,7]</sup> that is spectrally very well separated from an efficient, long-lived photoluminescence (i.e., a very large Stokes shift).<sup>[8]</sup> This characteristic optical behavior makes I-III-VI<sub>2</sub> NCs the most promising chromophores for efficient LSCs, combining effective harvesting of the solar spectrum and reabsorption-free waveguiding of the propagating luminescence. As a result, efficient solar concentration has been demonstrated in large area devices<sup>[2,9]</sup> that further feature neutral coloring particularly adapt for architectural integration of LSCs as, i.e., PV windows.<sup>[2a,10]</sup> Despite tremendous


advancements in this field, the fundamental photophysics of I-III-VI<sub>2</sub> NCs is still not fully understood, in particular concerning the long luminescence decay time and the characteristic wide global Stokes shift,  $\Delta_{\text{GS}}^{\text{G}}$ , between the absorption and emission spectra,<sup>[11]</sup> resulting in the lack of clear design guidelines

## 1. Introduction

Ternary semiconductor nanocrystals (NCs) of I-III-VI<sub>2</sub> composition, such as CuInS<sub>2</sub>, AgInS<sub>2</sub>, or CuGaSe<sub>2</sub>, are attracting considerable interest for numerous energy and optoelectronic

A. Anand, M. L. Zaffalon, C. Capitani, Dr. V. Pinchetti, Prof. F. Meinardi, Prof. S. Brovelli  
Dipartimento di Scienza dei Materiali  
Università degli studi di Milano-Bicocca  
Via Roberto Cozzi 55, IT-20125 Milano, Italy  
E-mail: francesco.meinardi@unimib.it; sergio.brovelli@unimib.it  
Dr. G. Gariano, Dr. M. Gandini, C. Capitani, Dr. F. Bruni  
Glass to Power SpA  
Via Fortunato Zeni 8, IT-38068 Rovereto, Italy

Dr. A. Camellini, Prof. M. Zavelani-Rossi  
Dipartimento di Energia  
Politecnico di Milano  
Via Ponzio 34/3, IT-20133 Milano, Italy  
Dr. R. Brescia  
Istituto Italiano di Tecnologia  
Via Morego 30, IT-16163 Genova, Italy  
Prof. M. Zavelani-Rossi  
IFN-CNR  
Piazza Leonardo da Vinci 32, IT-20133 Milano, Italy  
Dr. S. A. Crooker  
National High Magnetic Field Laboratory  
Los Alamos National Laboratory  
Los Alamos, NM 87545, USA

 The ORCID identification number(s) for the author(s) of this article can be found under <https://doi.org/10.1002/adfm.201906629>.

DOI: 10.1002/adfm.201906629

for their optimization. As discussed in the following, the term “global” is used here to indicate that, in contrast to the norm, the electronic transitions determining the spectral energies for absorption and emission in I–III–VI<sub>2</sub> are not the same.<sup>[11,12]</sup> Mostly based on the similarity between the luminescence spectral shape, lifetime, and Stokes shift of CuInS<sub>2</sub> NCs and those of copper doped II–VI NCs<sup>[11,13]</sup>—and by analogy those of AgInS<sub>2</sub> to silver-doped chalcogenides<sup>[13b,14]</sup>—most studies to date have considered the photoluminescence (PL) to arise from the radiative recombination of a conduction band (CB) electron with a hole localized in copper-related defects.<sup>[2a,15]</sup> Experimental support to this argument was provided by spectroscopic,<sup>[8a,15a,16]</sup> spectro-electrochemical<sup>[17]</sup> and electrical<sup>[5b]</sup> methods. Magneto-optical<sup>[18]</sup> experiments further revealed marked temperature-dependent Zeeman splitting due to sp–d exchange interaction between band-edge carriers and paramagnetic Cu<sup>2+</sup> cations (with 3d<sup>9</sup> electronic configuration) in both Cu-doped II–VI NCs and nonstoichiometric CuInS<sub>2</sub> NCs (Cu/In ratios between 1.25 and 1.45).<sup>[18,19]</sup> Strongly nonlinear magnetic field dependence of the circular polarization-resolved emission observed in both Cu:ZnSe NCs and CuInS<sub>2</sub> NCs<sup>[13a,18]</sup> with respect to the linear trend typically found in undoped CdSe NCs, further corroborated the picture that emission from nonstoichiometric CuInS<sub>2</sub> NCs involves localized dopant or defect states that feature a complex splitting of their level structure in applied magnetic fields. According to this picture, single particle experiments on copper deficient CuInS<sub>2</sub> NCs (1:2 Cu/In precursor ratio) by Zang et al.<sup>[16c]</sup> revealed markedly narrower single NC PL spectra with respect to the ensemble (60 meV vs 400 meV) that, together with the weak temperature dependence of the PL linewidth,<sup>[17a,20]</sup> suggest that the broad ensemble PL spectrum is mostly determined by the energy distribution of defect acceptor sites among different particles. Recent transport measurements<sup>[5b]</sup> support this argument.<sup>[21]</sup> The same study further highlighted the presence of In-related substitutional and/or interstitial defects acting as donors in indium treated NCs, in agreement with the excitonic pathway mediated by donor defects proposed by Kraaz et al.<sup>[22]</sup> and Leach et al.<sup>[23]</sup> An alternative interpretation ascribes the photophysics of CuInS<sub>2</sub> NCs to the recombination of self-trapped excitons featuring a strongly localized hole in the highest occupied molecular orbital due to the 3d states of Cu<sup>+</sup> cations.<sup>[13a,24]</sup>

However, a recent theory by Efros and co-workers<sup>[12]</sup> proposes a very different possibility, namely that the characteristic broadband optical absorption spectrum, long PL lifetimes and wide  $\Delta_{SS}^G$  can be explained by the structure of the valence band (VB). Specifically, effective mass calculations highlight a VB structure featuring low-energy odd parity hole sublevels of p-type symmetry (corresponding to the high energy VB sublevel depicted in red in the single electron diagram of Figure 1a) separated by a splitting energy,  $\Delta_{EO}$ , from higher-lying even parity hole levels (corresponding to the green VB sublevel in Figure 1a), whose wavefunctions have s-type contributions. As a result of the parity selection rules, the absorption spectrum is dominated by the optical transition between the even hole VB sublevel with total angular momentum  $F = 1$  and the 1S<sub>e</sub> electron level (blue arrow in Figure 1a), also featuring a s-type symmetry. On the other hand, the long-lived PL (black arrow in Figure 1a) arises from the parity-forbidden radiative transition

of the 1S<sub>e</sub> electron into the odd VB state also featuring  $F = 1$ . A recent work<sup>[25]</sup> provided experimental support for such a VB structure picture by showing the presence of an intense two-photon absorption transition below the one-photon absorption band edge. However, the PL of such NCs was suggested to still occur via a defect-mediated pathway, resulting in size and shape independent  $\Delta_{SS}^G$ , similarly to what observed by Xia et al.<sup>[16a]</sup> and Grandhi et al.<sup>[26]</sup> and commonly exhibited by Cu-doped CdSe NCs.<sup>[27]</sup>

Importantly, the model by Efros and co-workers (hereafter indicated as the VB structure model) makes testable predictions:<sup>[12]</sup> the quadratic decrease of  $\Delta_{SS}^G$  with the particle radius,  $a$ , and the linear growth of the radiative decay rate with  $a^2$ . These distinctive size dependences of the spectral and dynamical properties of I–III–VI<sub>2</sub> NCs arise from the linear proportionality of the admixture between the odd and even parity states with  $a$ . Specifically, as schematically depicted in Figure 1b (bottom panel), small CuInS<sub>2</sub> NCs exhibit a large  $\Delta_{EO}$  and negligible absorption from the odd parity VB sublevels (highlighted in red) featuring vanishingly small oscillator strength, thus resulting in a large  $\Delta_{SS}^G$ . Upon increasing the NCs size, odd and even parity sublevels come closer in energy,<sup>[12]</sup> resulting in a linear trend of  $\Delta_{EO}$  with  $a^{-2}$ . The resulting intermixing between such states intensifies the low energy absorption tail in large NCs (top panel in Figure 1b) which ultimately leads to the linear dependence of  $\Delta_{SS}^G$  on  $a^{-2}$ . On the same lines, increasing intermixing between VB substates should result in the linear growth of the radiative decay rate with  $a^2$ . To date, however, no study has experimentally investigated such spectroscopic signatures, leaving the model without direct experimental validation. Crucially, this photophysical scenario and in particular the progressive reduction of  $\Delta_{SS}^G$  in larger NCs, would have important implications for the use of CuInS<sub>2</sub> NCs as reabsorption-free emitters in LSCs. This is because the wide solar coverage (SC) enabled by low bandgap (large size) NCs with broadband absorption extending the near-IR region would be accompanied by stronger reabsorption losses of the propagating luminescence with respect to smaller NCs, due to the larger overlap with the respective emission spectrum. This behavior is shown in Figure 1c for representative CuInS<sub>2</sub> NCs with different particle size ( $a = 2.2$  nm vs  $a = 1.0$  nm) discussed in detail later in this work. On the other hand, whilst small NCs would be less affected by reabsorption (Figure 1c, bottom panel) their SC would be limited to the visible spectral region. This would limit the maximum achievable device efficiency and result in colored LSC panels which are not ideal for building integrated PV technologies. If the VB structure model is confirmed, the realization of efficient LSCs with simultaneously optimized solar harvesting and light concentration efficiency based on CuInS<sub>2</sub> NCs would require identifying the tradeoff between such antithetical size effects.

In this work, we aim to test the VB structure model by performing optical and magneto-optical investigations on stoichiometric CuInS<sub>2</sub> NCs of varying sizes. Consistently with the model, optical absorption and transient transmission measurements reveal the gradual broadening of the absorption tail, resulting in the linear increase of  $\Delta_{SS}^G$  with  $a^{-2}$ . Importantly, this behavior is accompanied by the linear growth of the PL radiative decay rate with  $a^2$ , also in agreement with the excitonic mechanism

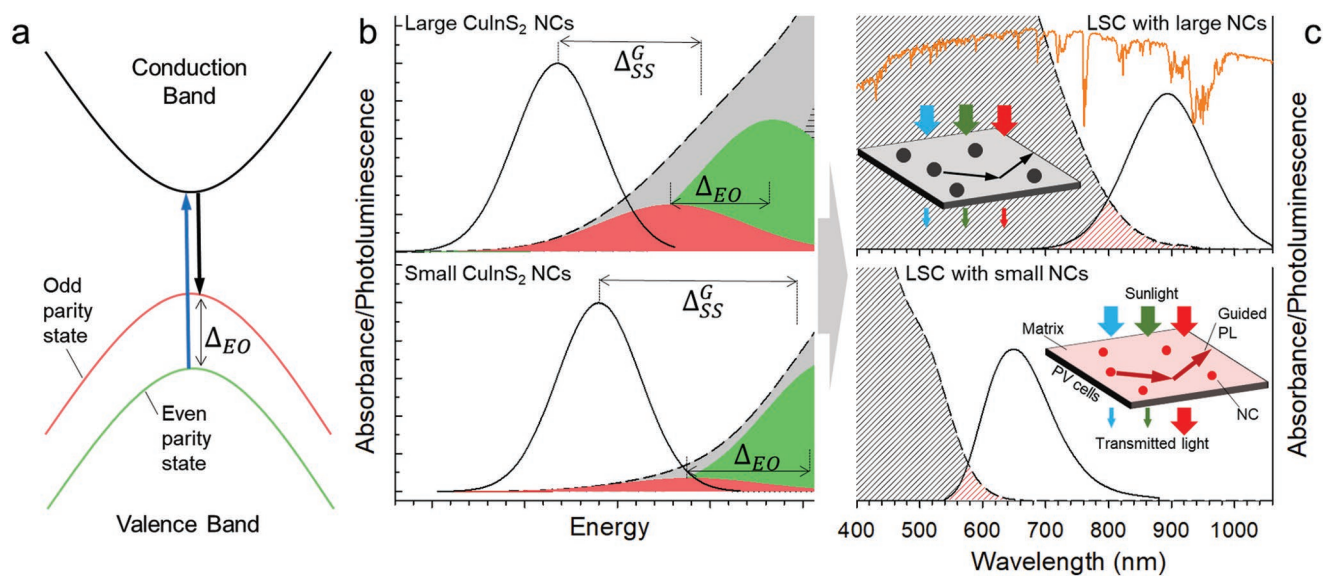


**Figure 1.** a) Schematic depiction of the band structure of  $\text{CuInS}_2$  NCs featuring odd and even parity VB sublevels separated by  $\Delta_{EO}$ . Optical absorption (blue arrow) is dominated by the electronic transition coupling the even VB sublevel and the CB, whereas luminescence (black arrow) occurs by parity forbidden radiative decay of the electron into the odd VB sublevel. b) Representative optical properties for large (top) and small (bottom)  $\text{CuInS}_2$  NCs as predicted by the VB structure model.<sup>[12]</sup> In small particles,  $\Delta_{EO}$  is large resulting in small intermixing between the VB substates and negligible oscillator strength coupling the odd parity VB substates and the CB (represented by the weak red absorption band). The absorption spectrum is dominated by the even parity substates (green band), the resulting  $\Delta_{SS}^G$  is large and the low-energy absorption tail is weak.  $\Delta_{EO}$  drops in larger NCs leading to larger intermixing between the VB substates and consequent broader low-energy absorption tail and smaller  $\Delta_{SS}^G$ . c) Side-by-side comparison between the normalized PL (solid black lines, excitation at 400 nm) and optical absorption (dashed black lines) spectra of stoichiometric  $\text{CuInS}_2$  NCs with radius  $a = 2.2$  nm (top panel) and  $a = 1.0$  nm (bottom panel). The absorption profiles are normalized to 1 optical density at the respective band-edge energy evaluated from the transient transmission spectra reported in Figure 2. The spectral overlap between the absorption and PL profiles are highlighted by red shading to emphasize the effect of broadened absorption tail with increasing  $a$  resulting in stronger reabsorption. Insets: schematic depiction of the LSCs under solar irradiation showing uniform spectral coverage for devices embedding large NCs resulting in no spectral distortion of the transmitted light. LSCs featuring small NCs instead transmit a larger fraction of the solar spectrum above 600 nm resulting in tinted devices and low color rendering index of the transmitted light.

proposed in ref. [12]. In addition to this, PL measurements below  $T \sim 50$  K show a 100-fold lengthening of the PL decay time, but no change in the PL quantum yield ( $\Phi_{\text{PL}}$ ), pointing to a further fine structure of the emitting band-edge exciton state, with splitting that scales as  $a^{-3}$ . Such a photophysics had so far never been observed in I-III-VI<sub>2</sub> NCs and is similar to what is well known in conventional II-VI NCs,<sup>[28]</sup> suggesting that also in this class of semiconductor NCs the fine structure of the first exciton manifold might emanate from enhanced exchange interaction.<sup>[29]</sup> Crucially, side-by-side time-resolved PL measurements on nonstoichiometric  $\text{CuInS}_2$  NCs and Cu-doped CdSe NCs of comparable size show exclusively the lengthening of the PL lifetime with decreasing temperature due to gradual suppression of thermally assisted nonradiative decay, strongly indicating that the observed fine structure effect derives from the very nature of the intrinsic band-edge exciton of defect-free  $\text{CuInS}_2$  NCs. In order to evaluate the implications of the observed size dependence of the optical properties of  $\text{CuInS}_2$  NCs on their use as LSC emitters, we performed Monte Carlo ray-tracing simulations based on the experimental spectra. The calculations highlight the interplay between the positive effect of wider solar harvesting with increasing particle size and the detrimental stronger optical losses by reabsorption, thus suggesting guidelines for device optimization. Based on such indications, we finally fabricated and tested a large area (30 cm × 30 cm) plastic LSC device embedding stoichiometric

$\text{CuInS}_2$  NCs with optimal size. By optically coupling such a device with c-Si solar cells, we achieved record optical power efficiency (OPE) of 6.8% that further confirms the technological relevance of our fundamental findings.

## 2. Results and Discussion

### 2.1. Synthesis and Optical Properties of Stoichiometric $\text{CuInS}_2$ NCs

$\text{CuInS}_2$  NCs were synthesized following the heat-up procedure described in the Methods section that ensures production of stoichiometric particles by suitably tuning the reactant concentration.<sup>[6b,8a,16b,24]</sup> When a precursor ratio of 1:1 In:Cu was used,  $\text{CuInS}_2$  NCs with In:Cu:S stoichiometric ratios close to 1:1:2 were obtained, as confirmed by inductively coupled plasma atomic emission spectroscopy (ICP-AES) analysis indicating a composition of  $\text{Cu}_{1.04}\text{In}_{2.01}\text{S}_4$ . The  $\text{CuInS}_2$  NCs present tetragonal chalcopyrite-like structure (Figure S1, Supporting Information). Transmission electron micrographs (TEM) of two representative aliquots are reported in Figure S2 (Supporting Information) showing size distribution consistent with previous reports.<sup>[16a,30]</sup> High-resolution TEM (HR-TEM) images of representative NCs in the two chosen samples mostly show spheroidal particles, rather than well-faceted shapes,

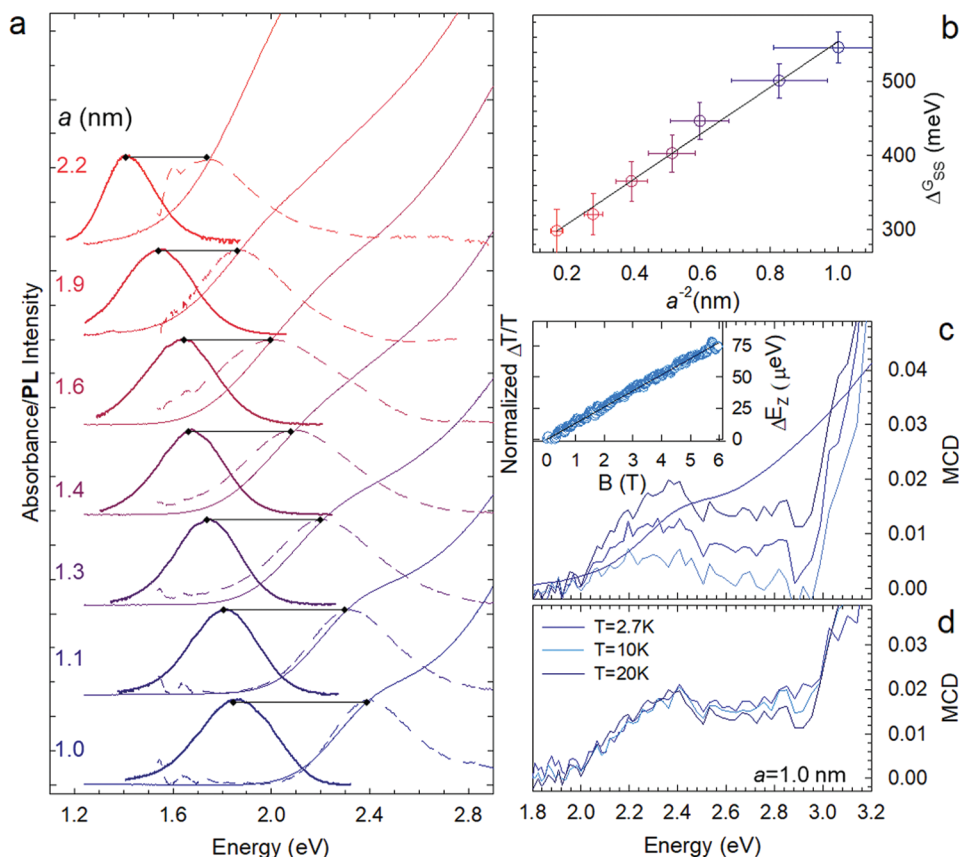


**Figure 2.** a) Optical absorption (thin solid lines), PL spectra (bold solid lines) and normalized transient transmission (TT, dashed lines) spectra at 10 ps pump–probe delay of CuInS<sub>2</sub> NCs with increasing mean radius  $a$ . The global Stokes shift values,  $\Delta_{SS}^G$ , between the absorption and PL spectra of each NC sample are indicated by black bars and reported as a function of  $a$  in panel (b).  $\Delta_{SS}^G$  extracted as the energy difference between the peak energy of the TT and PL spectra in panel “a” as a function of the particle size  $a$ . c) MCD of CuInS<sub>2</sub> NCs at 2.7 K and increasing magnetic field ( $B = 2, 4, 6$  T). The linear absorption at 2.7 K is shown as a bold blue line. Inset: Zeeman splitting of the band-edge exciton versus magnetic field together with the fit to the linear Zeeman splitting function (black line,  $R^2 = 0.994$ ). d) MCD of CuInS<sub>2</sub> NCs at 6 T showing no temperature dependence for  $T = 2.7$ –20 K.

especially in the smaller NCs. This holds in particular for the smallest NCs (not shown here), which are harder to identify even by HR-TEM imaging, due to the low number of atoms, which hardly stabilize in an ordered (i.e., crystalline) structure, thus in an anisotropic shape.

We start our analysis by looking at the optical spectra of the CuInS<sub>2</sub> NCs reported in Figure 2a. The spectra show the characteristic broadband absorption profile and the Stokes-shifted PL of I–III–VI<sub>2</sub> NCs progressively moving to lower energy with increasing particle radius. According to previous reports, the absorption spectra show no discernible first excitonic peak, but exclusively a low energy shoulder.<sup>[3d,16a,31]</sup>

To most accurately determine the spectral position of the dominant absorption feature, we performed transient transmission (TT) measurements. The TT spectra measured at low excitation fluence—when the number of photons absorbed per NC per pulse ( $\langle N \rangle$ ) is much less than unity (dashed lines in Figure 2a)—are dominated by a bleaching band due to the saturation of band-edge states where carriers accumulate following intraband relaxation.<sup>[2a,8a]</sup> The bleaching peak energy is used to extract the mean particle radius for the various NC aliquots by using the sizing curve provided in ref. [16]. The obtained NC

radii for the largest NCs for which reliable TEM images can be obtained, agree with the particle size estimated from the analysis of the respective micrographs reported in Figure S2 (Supporting Information). The peak energy of each TT spectrum that identifies the “center of mass” of the low energy absorption due to the interplay between  $\Delta_{E0}$  and the respective oscillator strength of the even and odd parity VB sublevels shifts toward the low energy portion of the respective absorption spectrum with increasing  $a$ . This is consistent with the VB structure model predicting a larger contribution from the odd VB sublevels in larger particles (Figure 1a) progressively broadening the absorption tail. As a result,  $\Delta_{SS}^G$  extracted as the energy difference between the bleaching maximum and the respective PL peak (black bars in Figure 2a) reported in Figure 2b increases linearly with  $a^{-2}$ , in agreement with the theoretical prediction.<sup>[12]</sup> This represents a first experimental evidence of the VB structure origin of the Stokes-shifted PL in stoichiometric I–III–VI<sub>2</sub> NCs where the radiative exciton decay does not necessarily involve an intragap defect state.

As anticipated above, previous magneto-optical studies on nonstoichiometric CuInS<sub>2</sub> NCs revealed the presence of paramagnetic species in the NC, likely associated



with copper-related defects,<sup>[18]</sup> similar to what observed in II–VI chalcogenide NCs doped with group-11 transition metals.<sup>[14,19,32]</sup> Therefore, magneto-optical experiments can be used to corroborate the absence (or reveal the presence) of such states in our stoichiometric NCs. With this in mind, we performed magnetic circular dichroism (MCD) measurements as a function of temperature and magnetic field.<sup>[33]</sup> In Figure 2c, we report the MCD spectra of CuInS<sub>2</sub> NCs ( $a = 1.0$  nm) at increasing magnetic field up to  $B = 6$  T at 2.7 K, together with the corresponding linear absorption spectrum (analogous data for CuInS<sub>2</sub> NCs with  $a = 2.2$  nm is reported in Figure S3 in the Supporting Information). The MCD spectrum shows one main peak at  $\approx 2.35$  eV corresponding to the NC's absorption shoulder that intensifies with increasing magnetic field. In the inset of Figure 2c, we report the extracted Zeeman splitting energy ( $\Delta E_Z$ ) growing linearly with the magnetic field thus suggesting the absence of paramagnetic species in these NCs (details on the procedure for extracting  $\Delta E_Z$  are reported in the Supporting Information). Accordingly, these data are perfectly fitted with the linear Zeeman splitting function  $\Delta E_Z = \mu_B F B g_{EX}$ , where  $\mu_B$  is the Bohr magneton and  $g_{EX}$  is the Landé factor of the band-edge exciton responsible for optical absorption (mostly formed by a hole in the even VB substate and a CB electron). The obtained  $g$ -factor,  $g_{EX} = 0.22$ , also found for NCs with  $a = 2.2$  nm (Figure S3, Supporting Information), is in agreement with previous results on CuInS<sub>2</sub> NCs.<sup>[18]</sup> Most importantly, the magnetic response of the absorption peak (Figure 2d) is found to be temperature independent, in contrast to the

temperature-dependent MCD that was observed in nonstoichiometric CuInS<sub>2</sub> due to paramagnetic defects.<sup>[18]</sup> Therefore, MCD data further corroborate the picture that the photophysical behavior of our stoichiometric CuInS<sub>2</sub> NCs is intrinsic.

## 2.2. Temperature-Controlled Time-Resolved Photoluminescence Experiments

Further support to the VB structure model emerges from the analysis of the exciton decay kinetics with increasing  $a$ . As anticipated above, within this model, gradual intermixing between the VB substates results in an  $a^2$ -dependence of the radiative decay rate,  $k_{RAD}$ . To experimentally evaluate this effect, we performed steady state and time-resolved PL experiments. Since the  $\Phi_{PL}$  and decay kinetics of CuInS<sub>2</sub> NCs are known to be strongly affected by temperature-dependent nonradiative processes,<sup>[17a]</sup> we conducted our experiments at decreasing temperature from 300 to 5 K. This enables us to suppress phonon-assisted nonradiative decay phenomena and thereby evaluate the evolution of  $k_{RAD}$  versus  $a$ .

To start with this part of the analysis, in Figure 3a we report the  $\Phi_{PL}$ -values of five representative CuInS<sub>2</sub> NCs with increasing size ( $a = 1.0, 1.4, 1.6, 1.9,$  and  $2.2$  nm) from 300 to 5 K. The inset shows the evolution with  $T$  of the PL spectra of the  $a = 1.0$  nm NCs.  $\Phi_{PL}$  of all systems increases with decreasing  $T$ , reaching saturation at  $\approx 100$  K, thus confirming the presence of temperature-activated nonradiative channels that are suppressed at lower  $T$ . We label the  $100 \text{ K} \leq T \leq 300 \text{ K}$  interval as

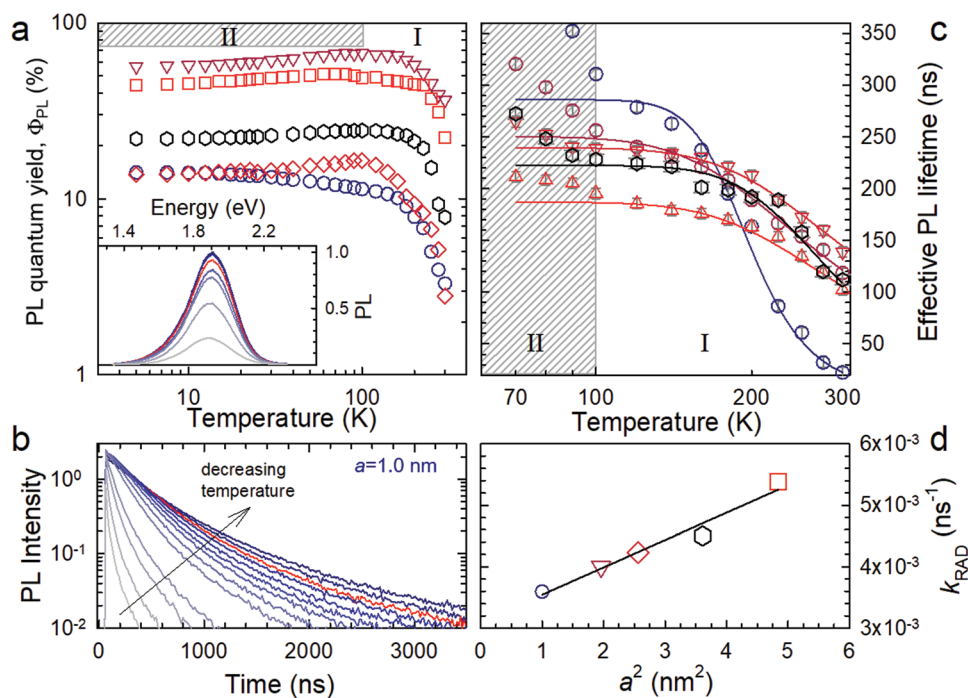


**Figure 3.** a)  $\Phi_{PL}$  as a function of temperature of CuInS<sub>2</sub> NCs of increasing size,  $a = 1.0$  (circles), 1.4 nm (triangles), 1.5 nm (diamonds), 1.9 nm (hexagons), and 2.2 nm (squares). Inset: PL spectra of CuInS<sub>2</sub> NCs with  $a = 1.0$  nm at decreasing temperature (from gray to dark blue). The red line corresponds to  $T = 100$  K. b) PL decay curves of NCs having  $a = 1.0$  nm at decreasing temperature (indicated by the black arrow). The red line corresponds to  $T = 100$  K. c) Effective PL decay times as a function of temperature (from 300 to 70 K) of the same CuInS<sub>2</sub> NCs as in panel “a” together with the respective fitting curves to Equation (1). d)  $k_{RAD}$  of the whole set of CuInS<sub>2</sub> NCs showing quadratic growth with  $a^2$  in agreement with predictions from ref. [12]. The black line represents the linear fit of  $k_{RAD}$  versus  $a^2$ .

range I. For lower temperatures (range II),  $\Phi_{\text{PL}}$  is largely constant for all systems. Consistently with previous reports, the efficiency losses in range II are ascribed to ultrafast trapping of photocarriers by surface defects in the absence of a wide gap passivating shell that result in a subpopulation of nonemissive NCs in the ensemble.<sup>[17a]</sup> We highlight that, for this study, we preferred to investigate exclusively core-only CuInS<sub>2</sub> NCs, as the overgrowth of a protecting wide bandgap shell, such as ZnS,<sup>[31]</sup> typically leads to the formation of alloyed quaternary particles by diffusion of Zn, which modifies the electronic structure of the core.<sup>[6b,16c,17a]</sup> Nevertheless, the invariance of  $\Phi_{\text{PL}}$  of our particles in range II confirms the temperature-independence of surface trapping and indicates that the photophysics for  $T \leq 100$  K discussed later in this work is due to purely radiative phenomena occurring in surface trapping-free NCs.

Looking first at the PL decay curves in range I (Figure 3b) for NCs with  $a = 1.0$  nm, we observe the typical multiexponential kinetics of unshelled CuInS<sub>2</sub> NCs that progressively slows down with decreasing  $T$  with no measurable variation of the zero-delay intensity, in agreement with the temperature independence of ultrafast charge trapping channels depleting the NC bands faster than our temporal resolution.<sup>[17a]</sup> Importantly, for  $T$  close to 100 K the PL decay curves accumulate indicating that the PL process is approaching its radiative regime.

To better monitor the evolution of the PL kinetics in range I and to evaluate the radiative decay time as a function of  $a$ , in Figure 3c we report the respective effective PL lifetimes ( $\tilde{\tau}$ ) extracted as the time after which the PL intensity drops by

$1/e$ . At room temperature, the  $\tilde{\tau}$ -values of the various NCs are uncorrelated to their respective  $\Phi_{\text{PL}}$ , consistent with the major nonradiative channel being ultrafast carrier trapping that renders a subpopulation of NCs nonemissive without affecting the PL lifetime of the emissive particles. More importantly, in accordance with the  $\Phi_{\text{PL}}$  trends,  $\tilde{\tau}$  of all NCs increases and reaches a nearly constant value for  $T \approx 100$  K, based on which we ascribe such a lifetime to the effective radiative exciton decay time,  $\tilde{\tau}_{\text{RAD}} = 1/k_{\text{RAD}}$ , of the bright subpopulation of NCs in the ensemble. To evaluate  $\tilde{\tau}_{\text{RAD}}$  for our NCs, we performed a global fit of the  $\tilde{\tau}$  versus temperature trends in range I using the equation:  $\tilde{\tau}^{-1} = \tilde{\tau}_{\text{RAD}}^{-1} + \tau_{\text{NRAD}}^{-1}(T)$ , that neglects ultrafast surface trapping and describes the nonradiative decay rate by the standard displaced harmonic oscillator model<sup>[34]</sup>

$$\tau_{\text{NRAD}}^{-1}(T) = A * \exp(-E_A/(k_B T)) \quad (1)$$

Through this fit, we obtain activation energies for the nonradiative decay of  $E_A \approx 70 \pm 4$  meV. More importantly for our purposes, the  $k_{\text{RAD}}$ -values obtained through the fitting procedure grow linearly with  $a^2$  (Figure 3d), in agreement with theoretical expectations based on the VB structure model.

A closer look at the lowest temperature values in Figure 3c, highlighted by the gray patterned area and corresponding to constant values of  $\Phi_{\text{PL}}$ , reveals further increase of  $\tilde{\tau}_{\text{RAD}}$  for  $T < 100$  K that is particularly evident for the smallest NCs in the set. This additional temperature trend becomes evident by looking at the time-resolved PL data in range II shown in Figure 4

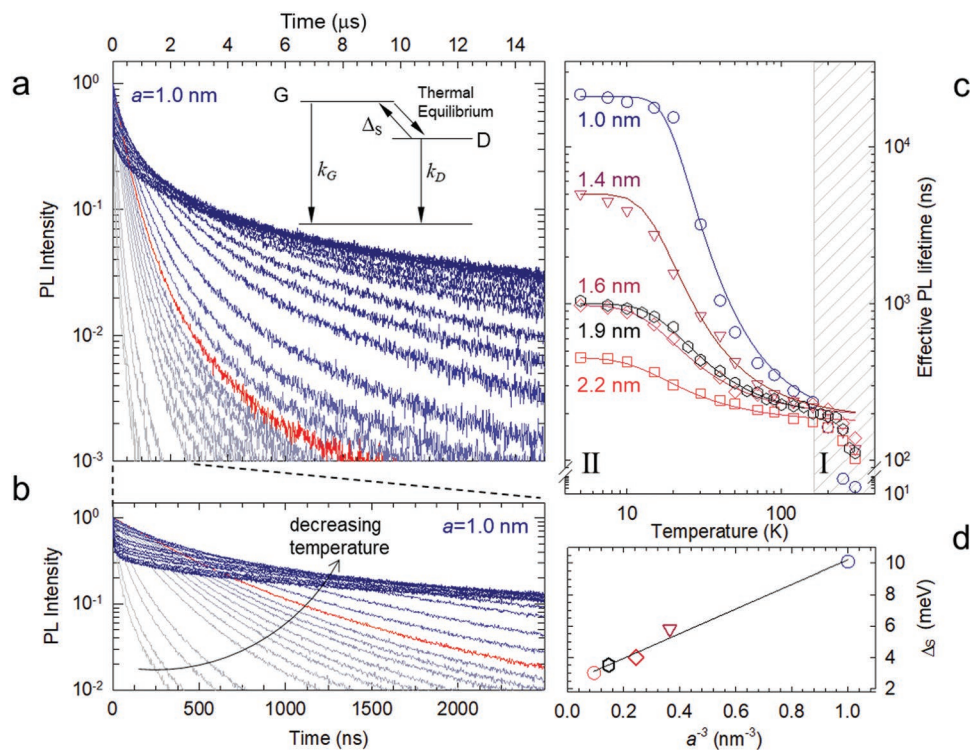


**Figure 4.** a) PL decay curves for CuInS<sub>2</sub> NCs ( $a = 1.0$  nm) at decreasing temperature from 300 to 5 K (from gray to blue). The red line corresponds to  $T = 100$  K. Inset: Three-level model of gray (G) and dark (D) exciton states separated by energy  $\Delta_S$ . b) Enlargement of the initial portion of the PL decay versus  $T$  highlighting the appearance of the initial fast portion for  $T$  below 100 K. c) Effective PL decay lifetimes of CuInS<sub>2</sub> NCs of increasing size as a function of temperature together with the respective fits to Equation (2). d)  $\Delta_S$ -values extracted through the fitting procedure as a function of  $a^{-3}$ , highlighting the inverse volume dependence of the dark-gray splitting energy.

revealing the unexpected emergence of exciton fine structure effects in ternary I–III–VI<sub>2</sub> NCs. In Figure 4a, we report the PL decay traces for CuInS<sub>2</sub> NCs (*a* = 1.0 nm) across the entire range of investigated temperatures. The PL decay curve corresponding to 100 K is shown in red to highlight the accumulation of decay lines as the thermally assisted nonradiative losses are suppressed and to mark the passage from temperature range I to range II. Strikingly, by lowering the temperature further, the PL kinetics dramatically slows down and turns from multiexponential to markedly nearly double-exponential with an initial fast portion followed by a tens of microseconds long component, over two orders of magnitude slower than the radiative kinetics at ≈100 K. The effect is highlighted in Figure 4b where we zoomed-in the first two decades of signal in the first 2.5 μs of decay. This kind of kinetic behavior occurring at constant values of Φ<sub>PL</sub> has been widely reported for binary chalcogenide NCs, including CdSe,<sup>[28,29]</sup> CdTe,<sup>[35]</sup> ZnSe,<sup>[36]</sup> and their heterostructures (i.e., CdTe/CdSe or CdSe/CdS NCs)<sup>[37]</sup> as well as in PbSe<sup>[38]</sup> NCs, where the fast initial decay at low temperature has been ascribed to coupling of the ground state to a confined acoustic phonon or to the thermalization of excitons from a higher-energy optically allowed state (commonly referred to as the bright exciton) to a lower-lying optically forbidden (dark) exciton state. The much slower decay, on the other hand, arises from the radiative recombination of dark excitons in thermal equilibrium with the environment.<sup>[28a,37b]</sup> This decay becomes progressively faster with increasing temperature as a result of thermal excitation of dark excitons to the bright upper exciton state. Figure 4c reports the evolution of τ<sub>RAD</sub> with temperature for five CuInS<sub>2</sub> NC samples of increasing size extracted following the procedure used in range I and by neglecting the initial decay portion due to rapid thermalization in range II. For the smallest NCs, τ<sub>RAD</sub> approaches 20 μs at temperatures below ≈20 K and undergoes a two orders of magnitude decrease at higher temperatures (τ<sub>RAD</sub>(100 K) ≈ 250 ns).

In analogy to the behavior of CdSe NCs, we ascribe this effect to the thermal activation between two substates of the exciton fine structure having markedly different emission lifetime. Note that, in contrast to CdSe NCs, in CuInS<sub>2</sub> NCs both such states belong to the weakly allowed exciton consisting of a CB electron and a hole in the odd parity VB sublevel. Therefore, we adopt the language typically used to describe exciton states that are strongly and weakly forbidden by symmetry in transition metal dichalcogenide semiconductors<sup>[39]</sup> and label the long-lived exciton as dark and the higher lying emissive exciton as gray, so as to distinguish the current case from the norm, where the emissive state is optically allowed and therefore “bright.” By assuming a Boltzmann distribution of excitons between these two dark (D) and gray (G) states, we can model the transition between the slow and fast decay regimes in a simple three-level scheme (inset of Figure 4a), by expressing the radiative decay rate as

$$k_{\text{RAD}}(T) = \tilde{\tau}_{\text{RAD}}^{-1}(T) = (k_{\text{D}} + k_{\text{G}}e^{-\Delta_{\text{S}}/k_{\text{B}}T}) \left(1 + e^{-\Delta_{\text{S}}/k_{\text{B}}T}\right)^{-1} \quad (2)$$

where *k<sub>D</sub>* and *k<sub>G</sub>* are the radiative decay rates of dark and gray excitonic states respectively and Δ<sub>S</sub> being the respective splitting energy. The above model reproduces the experimental data well for all CuInS<sub>2</sub> NCs, yielding Δ<sub>S</sub>-values comparable

to those found in binary chalcogenide NCs of similar size (Figure 4d).<sup>[29a]</sup> Interestingly, as observed in CdSe NCs, Δ<sub>S</sub> is found to scale linearly with *a*<sup>-3</sup>, suggesting that also in CuInS<sub>2</sub> NCs the fine structure splitting energy follows the linear dependence with the inverse of the particles volume of the exchange energy of uncorrelated electron–hole pairs.<sup>[29b]</sup> Importantly, time-resolved PL measurements on off-stoichiometry Cu<sub>1-x</sub>In<sub>x</sub>S<sub>2</sub> (*x* = 0.8) and Cu:doped CdSe NCs with *a* = 1.0 nm shown in Figure S5 (Supporting Information) evidence no fine structure effects in neither system. This supports the picture that the excitation responsible for the optical properties of stoichiometric CuInS<sub>2</sub> nanocrystals is of different nature than the Cu-defect emission in both off-stoichiometry CuInS<sub>2</sub> NCs and in Cu:doped II-VI chalcogenides. It is also worth noting that time-resolved PL measurements at 5 K show nearly no acceleration of the PL kinetics upon the application of a magnetic field (*B* = 5 T; Figure S6, Supporting Information), as is instead observed in CdSe NCs due to magnetic mixing of the dark and bright exciton state Hamiltonians.<sup>[28b]</sup> We speculate that such an effect might be due to the optically forbidden nature of both the dark and gray excitons in CuInS<sub>2</sub> NCs resulting in substantial decrease of the coupling to external magnetic fields.

### 2.3. Implications on the LSC Performance and Optimization Strategies

The agreement between the size dependencies of the spectral and dynamical parameters observed for our CuInS<sub>2</sub> NCs with the theoretical predictions by Efros and co-workers<sup>[12]</sup> provide strong indications that the optical properties of stoichiometric ternary I–III–VI<sub>2</sub> NCs are due to the detailed structure of the VB. This has important implications for the application of this class of NCs to light management technologies and in particular to LSCs. These devices typically consist of optical waveguides coated or doped with chromophores that absorb sunlight and emit longer wavelength luminescence that propagates by total internal reflection to the device edges, where it is converted to electricity by PV cells installed along the device perimeter. Such an all-optical functioning mechanism makes LSCs particularly suitable for building integrated PV applications spanning from sound barriers<sup>[40]</sup> to coverages<sup>[41]</sup> and electrodeless solar windows,<sup>[42]</sup> and could even help architects in enhancing the aesthetic value of a building. As anticipated above, the realization of efficient LSCs relies of the combination of broadband optical absorption to ensure effective solar harvesting and minimized spectral overlap between the absorption and PL spectra of the chromophores, so as to suppress losses to re-absorption (other critical aspects are the optical quality and transmittance of the waveguide matrix<sup>[10]</sup> and the type of PV cells<sup>[43]</sup>).

For building integration and in particular for solar glazing applications, a further key parameter that is directly connected to the spectral coverage is the color of an LSC panel, which determines both the indoor-to-outdoor vision and the quality of the transmitted sunlight illuminating indoor settings. In the case of NCs featuring a continuous optical absorption spectrum, a large SC and a neutral coloring can be achieved by using particles featuring an absorption edge in the near infrared spectral region.<sup>[2a]</sup> However, in the case of the stoichiometric CuInS<sub>2</sub>



NCs discussed here, mitigation of quantum confinement in large particles is accompanied by the gradual reduction of  $\Delta_{SS}^G$ , resulting in stronger reabsorption of the propagating PL that is detrimental for the device efficiency. In order to evaluate the impact of such a behavior on the device performance, we used the optical absorption and PL spectra of the  $\text{CuInS}_2$  NCs with increasing  $a$  reported in Figure 2a to perform Monte Carlo ray-tracing simulations of light propagation in squared LSCs of increasing lateral dimension,  $L$  (thickness 0.5 cm). To avoid parasitic effects due to the different PL quantum efficiency of the NCs, in our calculations we imposed  $\Phi_{\text{PL}} = 95\%$  for all systems and neglected optical absorption by the matrix material, so as to focus exclusively on the NC properties. The LSC performance are evaluated by estimating the number of photons emitted from the waveguide edges, independently on the type of PV cells coupled to the device perimeter.

To evaluate the effect of the progressively smaller  $\Delta_{SS}^G$  and the broader low-energy absorption tail with increasing  $a$ , in Figure 5a,b we first compute the behavior of LSCs featuring the same absorbance below the effective bandgap energy of the respective NCs (corresponding to the peak energy of the 1S bleach in the TT spectra; Figure 2a). The SC of the various LSCs calculated in the 280–1100 nm wavelength range, corresponding to the maximum spectral portion exploitable by LSCs coupled to silicon PV cells, is shown in Figure 5c. Consistent with the evolution of the absorption spectra with  $a$ , the optical quantum efficiency—OQE, defined as the ratio between the number of photons emitted from the waveguide edges and the number of absorbed solar photons—of LSCs embedding large NCs drops with increasing device dimensions due to progressively stronger reabsorption losses (Figure 5a). However, as highlighted in Figure 5b by the optical efficiency (OE)

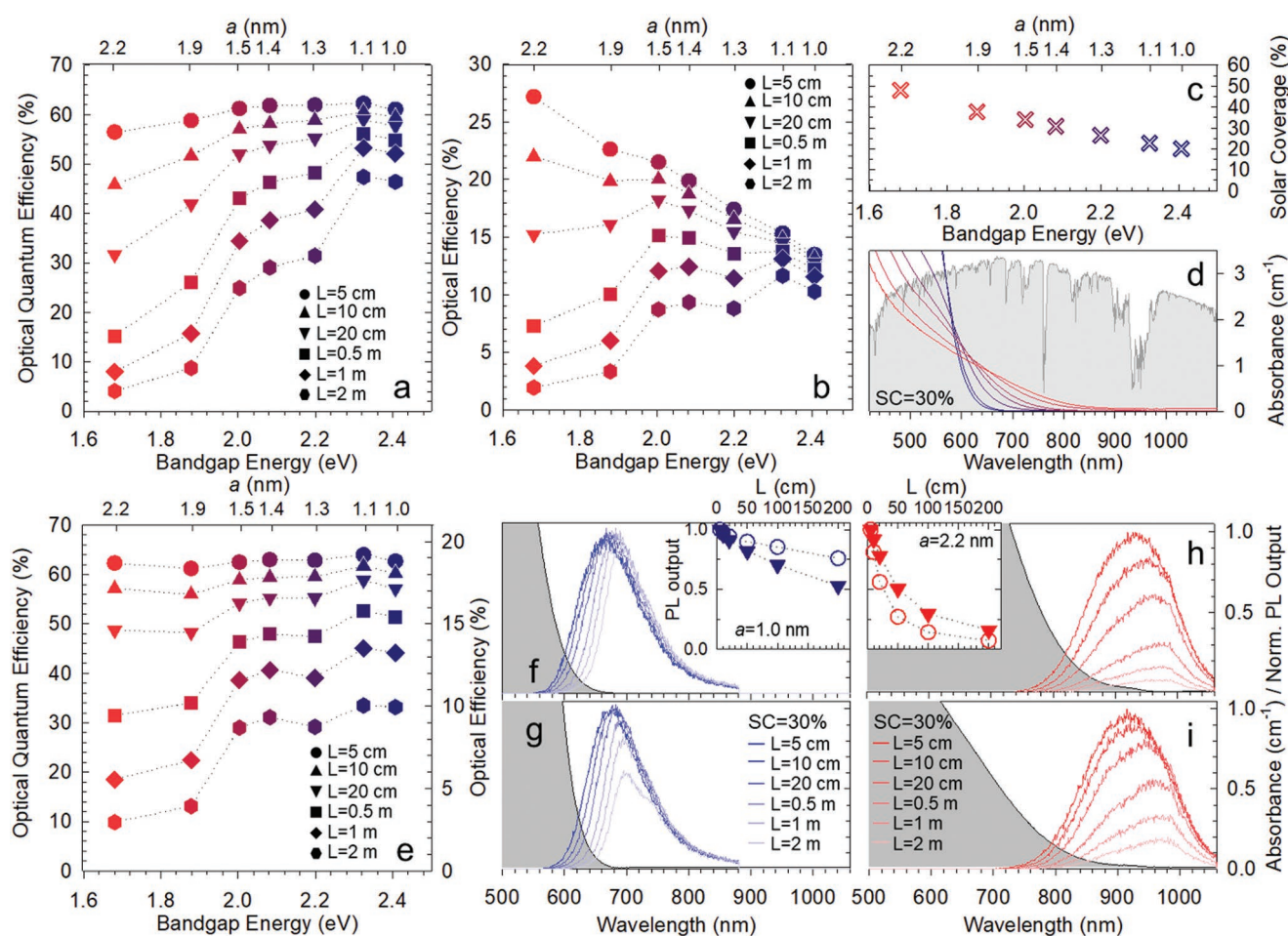


**Figure 5.** Monte Carlo ray-tracing calculation of the a) OQE and b) OE of squared LSCs (thickness 0.5 cm) with increasing lateral size ( $L$ ), embedding the  $\text{CuInS}_2$  NCs with different bandgap energy shown in Figure 2a. The simulated LSCs feature the same integrated optical absorption below the band edge of the respective NCs (defined as the peak energy of the 1S bleach in the TT spectra reported in Figure 2a). c) SC of the same devices as in “a” and “b” calculated in the 280–1100 nm wavelength range. d) Absorption spectra of LSCs based on the same  $\text{CuInS}_2$  NCs assuming identical spectral coverage of  $\text{SC} = 30\%$ . The AM 1.5G solar spectrum (expressed in photons  $\text{m}^{-2} \text{s}^{-1}$ ) used for the simulations is reported in gray. e) Calculated OQE and OE as a function of the NC size (bandgap energy) for LSCs with identical SC (30%) and increasing  $L$ . f, h) Edge-emitted PL spectra of NCs with  $a = 1.0$  nm (blue lines) and  $a = 2.2$  nm (red lines) embedded into LSCs with increasing  $L$  featuring the same below gap absorbance. The respective integrated PL intensities are shown respectively as blue and red circles in the insets of panels “f” and “h.” g, i) Edge-emitted PL spectra of the same LSCs in the case of equal spectral coverage,  $\text{SC} = 30\%$ . The respective integrated PL intensities are shown as blue and red triangles in the insets of panels “f” and “h.”



of the same devices—evaluated as the number of edge-emitted photons divided by the number of solar photons impinging on the device surface—this effect is partially mitigated by the progressively wider spectral coverage (SC) enabled by the use of larger NCs featuring a lower bandgap energy (Figure 5c). As a result, for small devices ( $L = 5$  cm, 10 cm) where average light propagation distances are relatively short, reabsorption losses play a minor role with respect to solar harvesting, resulting in the monotonic growth of the OE with increasing NC size, reaching  $OE > 20\%$  for  $L = 10$  cm, despite a relatively low solar coverage ( $SC < 40\%$ ). For larger  $L$ -values, reabsorption becomes the dominant parameter, gradually lowering the OE for LSCs embedding large NCs. Importantly, an optimum is found for large LSCs ( $L = 0.5$  m) embedding NCs with  $a = 1.5$  nm showing OE as high as 15%. Notably, nearly constant  $OE > 10\%$  versus  $a$  is calculated also for devices with  $1$  m<sup>2</sup> size, which would be particularly adapt for architectural integration. We stress that the use of NCs with  $a \geq 1.4$  nm has the key advantage of enabling the fabrication of LSC devices of neutral color, whose integration into glazing systems would introduce negligible distortion of the transmitted solar spectrum. For the devices discussed in this work, the transmitted sunlight would exhibit a Color Rendering Index,  $R_a > 90$ , that fulfils the highest requirements for indoor illumination (corresponding to CIE color rendering group 1A).

Having evaluated the effect on LSCs of stoichiometric CuInS<sub>2</sub> NCs with different size by considering equal bandgap absorptance (Figure 5a–c), we proceed with comparing the applicative potential of such NCs in the more realistic case of LSCs featuring the same solar harvesting capability, corresponding to  $SC = 30\%$ . The respective absorption spectra are shown in Figure 5d together with the AM 1.5G solar spectrum used for the simulations (expressed in photons m<sup>-2</sup> s<sup>-1</sup>). Consistent with the smaller bandgap and steeper low-energy absorption tail of small NCs ( $a < 1.3$  nm) due to negligible oscillator strength of the optical transition coupling the odd parity VB sublevel and the CB with respect to larger particles, the desired  $SC = 30\%$  is achieved with LSCs featuring a high NC loading, resulting in a sharp absorption edge at  $\approx 580$  nm. Upon increasing  $a$ , progressively lower NC contents are required for the same SC and the resulting absorption spectrum is gradually more uniform across the visible/near-IR region. As a consequence, for LSCs featuring the same spectral coverage, reabsorption losses are enhanced (reduced) in LSCs with small (large) particles than in the example discussed in Figure 5a,b that compared devices with equal absorptance at the bandgap of the respective NC emitters. This is testified by the OE (and OQE) trend of LSCs with increasing  $L$  in Figure 5e—for equal SC conditions, the OQE and the OE follow an identical trend as a function of  $a$  as highlighted by the double y-axis in Figure 5e—and by the side-by-side comparison of the edge-emitted PL spectra of LSCs based on NCs with  $a = 1.0$  nm and  $a = 2.2$  nm shown respectively in Figure 5f,g and Figure 5h,i. Specifically, the spread of the OE values versus  $L$  is narrower (wider) for  $a = 2.2$  nm ( $a = 1.0$  nm) in Figure 5e with respect to Figure 5a, which is consistent with the corresponding trends of the integrated PL output with the LSC dimension reported in the insets of Figure 5f,g, showing opposite behavior for the two different NC sizes. Most importantly, Figure 5e indicates that,

despite the significant transparency of 70%, OE as high as 12% could be achieved for large colorless LSCs ( $L = 1$  m) embedding NCs with  $a = 1.5$  nm and that increasing the device area to  $4$  m<sup>2</sup> would still yield efficiencies close to 10%.

#### 2.4. Highly Efficient Large-Area LSCs Based on Stoichiometric CuInS<sub>2</sub> NCs

Finally, to experimentally validate the design guidelines for efficient LSCs obtained from the Monte Carlo simulations, we fabricated prototype large-area semitransparent LSC devices ( $30$  cm  $\times$   $30$  cm  $\times$   $0.7$  cm, 60% absorptance in the 400–750 nm spectral range) that utilize stoichiometric CuInS<sub>2</sub> NCs. Based on the outcome of the theoretical modeling, we chose NCs with size  $a \approx 1.5$  nm, as they present the best tradeoff between broadband SC and suppressed reabsorption capability. Prior to encapsulation, the NCs were shelled with a 1 nm thick ZnS layer to protect their surfaces from the radical initiators used for the production of the polymeric waveguide. In agreement with previous reports, shelling substantially enhanced  $\Phi_{PL}$  from  $30 \pm 5\%$  to  $85 \pm 5\%$  without modifying the spectral properties of the NCs.<sup>[6c,31,44]</sup> The device was fabricated using the industrial cell-casting method for the production of optical grade poly(methyl methacrylate) (PMMA) waveguides free of scattering losses described in the Methods section.<sup>[45]</sup> The choice of PMMA as the waveguide material is dictated by its excellent optical properties,<sup>[10]</sup> high resistance to exposure to UV light, and various chemical treatments, as well as excellent performance in all-weather conditions. Figure 6a shows a photograph of the fabricated LSC containing 0.05 wt% of NCs under ambient illumination featuring the characteristic neutral brownish coloring well suited for architectural integration.<sup>[2a,b]</sup> The quality of the PMMA was assessed by gel permeation chromatography and nuclear magnetic resonance (NMR) spectroscopy indicating high average molar mass,  $M_n \approx 225$  000, and mass average molar mass,  $M_w \approx 240$  000, corresponding to a polydispersity value of 1.06, which indicates an extremely narrow chain length distribution. The amount of residual monomer in the final waveguides is  $<1\%$  in compliance with international safety requirements.

The optical absorption and PL spectra of the NCs in toluene solution and embedded into the PMMA waveguide are reported in Figure 6b, showing virtually identical spectral properties for the two samples (except for the absorption peak at 900 nm due to the vibrational overtone of the C–H stretching mode of the polymer). In agreement with previous reports,<sup>[2a]</sup> side-by-side PL efficiency measurements show that  $\Phi_{PL}$  of the pristine NCs is nearly completely preserved in the nanocomposite ( $\Phi_{PL}^{PMMA} = 80 \pm 5\%$ ). To quantitatively demonstrate the absence of scattering losses, in Figure 6c, we report the enlargement of the optical absorption spectrum in the spectral range corresponding to the PL spectrum. The background absorption is  $<1 \times 10^{-2}$  cm<sup>-1</sup> (with no arbitrary baseline subtraction), highlighting the absence of light scattering contributions.

This is confirmed by PL measurements in an integrating sphere on the same nanocomposite sample ( $3$  cm  $\times$   $3$  cm) with either clear or blackened edges, so as to distinguish between the light emitted from the LSC faces and the guided PL emitted

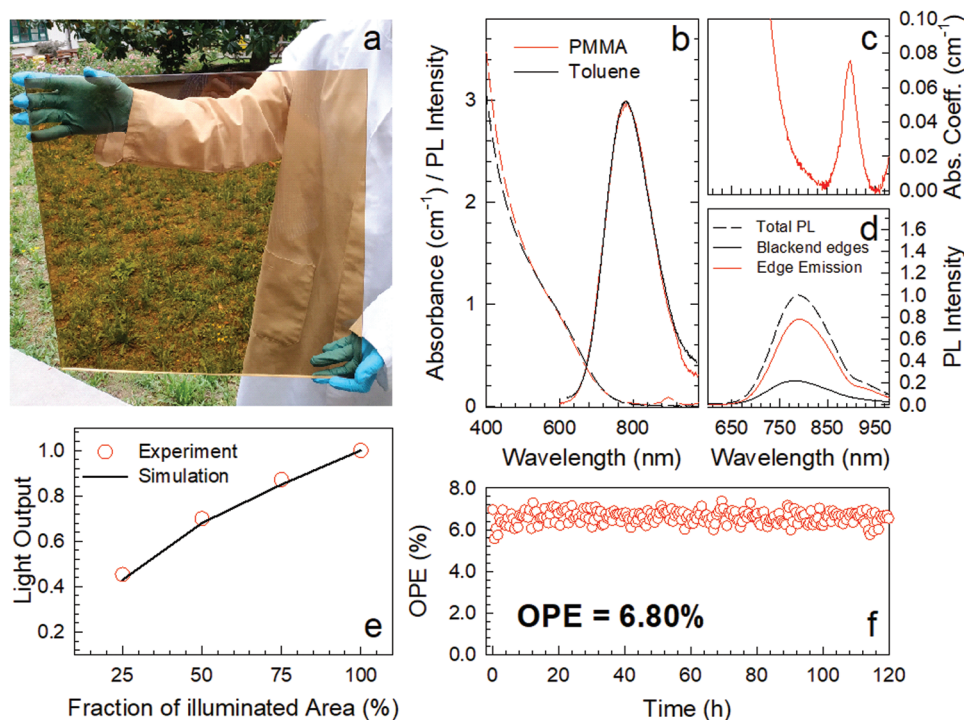


**Figure 6.** a) Photograph under daylight of an NC:PMMA (NCs embedded in PMMA) nanocomposite waveguide (400–750 nm transparency  $\approx 40\%$ , dimensions: 30 cm  $\times$  30 cm  $\times$  0.7 cm). b) Optical absorption (dashed lines) and PL (continuous lines) spectra of ZnS-capped CuInS<sub>2</sub> NCs ( $a = 1.5$  nm) in toluene solution (black curves) and embedded into a PMMA nanocomposite (red curves, NC concentration of 0.05 wt%). c) Enlargement of the absorption profile of the NC:PMMA LSC in the PL spectral region. No arbitrary baseline subtraction was applied to the data. d) PL spectra of a portion (3 cm  $\times$  3 cm) of the same LSC with the edges clear (total PL, black dashed line) and blocked by black paint (solid black line, corresponding to light emitted from the slab surface). The red line is the difference between the total PL and the surface emission and corresponds to the PL emitted from the waveguide edges. e) Relative optical output power measured from c-Si PVs coupled to one perimeter edge of the LSC as a function of the device area illuminated by a calibrated solar simulator (1.5 AM Global, circles). The theoretical trend obtained through Monte Carlo ray-tracing simulation of an ideal LSC with no scattering or reabsorption losses is reported as a black curve. f) Stability test under stress conditions: artificial sunlight illumination ( $\approx 1$  Sun); temperature of 55 °C. Point-to-point fluctuations in the OPE-values are due to oscillation in the intensity of excitation light.

from the slab edges. The PL data reported in Figure 6d show that the emission from the LSC edges corresponds to  $\approx 76\%$  of the total emission intensity, which closely matches the maximum theoretical value of light-trapping efficiency for a PMMA waveguide ( $\approx 74.1\%$  considering a refractive index of the polymer matrix  $n = 1.49$ ) defined by Snell's law. Having assessed the optical quality of our waveguide, we proceeded with quantifying the performances of our device by measuring the OE, the OQE and the OPE, defined as the ratio between the optical power emitted by the LSC and the incident solar power. For these measurements, we index-matched the perimeter edges ( $A_{\text{edge}} = 120 \text{ cm} \times 0.7 \text{ cm} = 84 \text{ cm}^2$ ) of the LSC shown in Figure 6a to calibrated c-Si solar cells and exposed the LSC to outdoors illumination perpendicular to its top surface ( $A_{\text{LSC}} = 30 \text{ cm} \times 30 \text{ cm} = 900 \text{ cm}^2$ ) and used a calibrated photodiode to instantaneously monitor the solar irradiance impinging onto the LSC top surface. No reflector or back diffuser was placed at the bottom of the waveguide. Based on these measurements, we obtained an  $\text{OPE} = 6.8 \pm 0.2\%$ , which is the highest optical power efficiency reported to date for a large area LSC. The corresponding OQE-value is 29.2%, corresponding to  $\text{OE} = 7.4\%$ . The effective mitigation of reabsorption losses using CuInS<sub>2</sub> NCs with  $a = 1.5$  nm, together with the absence of scattering losses, results in the nearly ideal behavior of the LSC.<sup>[46]</sup> This is

highlighted in Figure 6e, where we show the light output emitted from one of the device edges (30  $\times$  0.7 cm<sup>2</sup>) measured using the same setup adopted for the OE measurements (with only one slab edge coupled to the photodiodes and no back-reflector), but progressively exposing increasingly larger portions of the LSC area to the solar simulator. The same figure also reports the expected trend calculated using Monte Carlo ray-tracing simulation for an ideal scattering- and reabsorption-free device of identical dimensions embedded with emitters of the same  $\Phi_{\text{PL}}$  as the used NCs, in which the light output is determined exclusively by the numeric aperture of the illuminated device area. The experimental data are in very good agreement with the simulated trend, which supports the ascription that our LSC is close to an ideal device. Finally, to assess the stability of our stoichiometric CuInS<sub>2</sub> NCs and polymer waveguide in working conditions, we performed accelerated ageing test by exposing the LSC to continuous illumination with solar light at 55 °C. Remarkably, as shown in Figure 6f, the OPE of the LSC remains constant for over 120 h of continuous operation, thus further supporting the technological potential of our approach.

In conclusion, through the combination of optical and magneto-optical experiments on stoichiometric CuInS<sub>2</sub> NCs as a function of size and temperature we have revealed, for the first time, the spectroscopic signatures predicted for the excitonic

photophysics of I–III–VI<sub>2</sub> NCs. In agreement with effective mass calculations, measurements show quadratic dependence of the global Stokes shift and the radiative decay rate on the particle size, thus strongly supporting the theory by Efros and co-workers.<sup>[12]</sup> The absence of intragap defect states is consistent with magnetic circular dichroism experiments showing temperature independent MCD perfectly reproduced by the linear Zeeman splitting function. Time-resolved PL measurements performed below 50 K further reveal the dynamic signature of emission originating from a lower-lying dark-like exciton which are not found in Cu-doped CdSe NCs or off-stoichiometry CuInS<sub>2</sub> NCs. The splitting energy separating such a state from a gray exciton follows a linear trend with the inverse of particle volume as commonly observed in undoped II–VI chalcogenide NCs, suggesting that also in I–III–VI<sub>2</sub> NCs such a behavior originates from enhanced electron–hole spin interaction. We then evaluated the impact of the observed size dependence of the Stokes shift in stoichiometric CuInS<sub>2</sub> NCs on their suitability to LSCs, where I–III–VI<sub>2</sub> NCs are considered amongst the most promising candidates for high performance devices. Monte Carlo ray-tracing simulations enabled us to decouple the beneficial effect of progressively wider solar harvesting efficiency with increasing particle size from the concomitant detrimental increase of reabsorption losses in large area devices and thereby to suggest compromise optimization strategies to realize efficient LSCs with size and aesthetics compatible with building integrated PV applications. Based on such theoretical guidelines, we fabricated practical large-area LSC devices by embedding stoichiometric CuInS<sub>2</sub> NCs into mass polymerized PMMA waveguides. Thorough characterization of such a device revealed optical grade quality of the matrix and efficient NC emission, leading to an OPE as high as 6.8%, corresponding to the highest value reported to date for large-area LSC devices.

### 3. Experimental Section

**Materials:** Copper(I) iodide (CuI, purum, ≥99.5%), indium(III) acetate (In(OAc)<sub>3</sub>, 99.99%), 1-dodecanethiol (DDT, ≥98%), sodium myristate (≥99%), selenium powder-100 mesh (99.99%), oleic acid (OA, ≥90%), cadmium nitrate tetrahydrate (≥98%), copper(II) chloride dihydrate (99.999%), and 1-octadecene (ODE, ≥90%) were purchased from Sigma-Aldrich. Hexane (chromasolv, ≥97%), acetone (puriss. ≥99%), ethanol (puriss. ≥99%), and methanol (puriss. ≥99%) were purchased from Honeywell Riedel-de-Haën. All the chemicals were used without further purification. Methylmethacrylate (MMA, 99%, Aldrich), purified with basic activated alumina (Sigma-Aldrich), was used as a monomer for the preparation of polymeric nanocomposites. 2,2'-azobis(2-methylpropionitrile) (AIBN, 98%, Aldrich) and lauroyl peroxide (98%, Aldrich) were used as initiators without purification.

**Synthesis of CuInS<sub>2</sub> Nanocrystals:** For the synthesis of CuInS<sub>2</sub> NCs was followed a heat-up procedure.<sup>[6b,e,47]</sup> A mixture of CuI (0.4 mmol), In(OAc)<sub>3</sub> (0.4 mmol), and 5 mL of DDT was loaded into a three-neck flask and was degassed under vacuum at 130 °C for 1 h. In order to grow particles of different sizes, the temperature was initially raised to 230 °C to let the particles nucleate and grow. Aliquots were taken at different reaction times (2.5, 5, 10, 20, 30, 40, and 60 min) in order to obtain different nanocrystal sizes. Finally, the reaction was quenched by cooling the solution to room temperature. The NCs were cleaned by repeated precipitation with acetone and redispersion in hexane. In order to synthesize copper-deficient NCs (Cu:In = 1:4) was varied only the amount of the copper precursor (0.1 mmol).

**Synthesis of Cu:CdSe Nanocrystals:** For the synthesis of Cu:CdSe NCs was followed a heat-up procedure.<sup>[1]</sup> The Cd-myristate precursor was prepared via ex situ method: a solution of cadmium nitrate in methanol (0.05 M, 40 mL) was added to a solution of sodium myristate in methanol (0.025 M, 240 mL). The white precipitate was washed twice with methanol and dried under vacuum overnight to remove all solvents. 0.1 mmol (56 mg) Cd-myristate, 0.05 mmol (4 mg) Se powder, and 0.03 mmol (5 mg) copper chloride were added in a 25 mL flask with 6.38 mL of ODE and 1 mL of OA and exposed to vacuum for 30 min. Successively the mixture was heated to 210 °C for 45 min under nitrogen flow. The samples were finally purified twice with hexane/ethanol co-solvents by centrifugation (4500 rpm, 10 min) to remove excess ligands and unreacted precursor.

**Transmission Electron Microscopy:** High-resolution TEM (HR-TEM) and high-angle annular dark field-scanning TEM (HAADF-STEM) imaging was performed on an image-C<sub>s</sub>-corrected JEOL JEM-2200FS microscope (Schottky emitter), operated at an accelerating voltage of 200 kV.

**Powder X-Ray Diffraction:** Powder XRD patterns were acquired in Bragg–Brentano geometry with Cu K $\alpha$  radiation (Panalytical X'Pert Pro powder diffractometer).

**Inductively Coupled Plasma Atomic Emission Spectroscopy:** ICP-AES was carried out using an iCAP 6500 Thermo spectrometer. Samples were dissolved in HCl/HNO<sub>3</sub> 3:1 (v/v).

**Spectroscopic Studies:** Absorption spectra of NCs in solution were measured with a Cary 50 UV–vis spectrophotometer. Steady-state PL measurements were performed by exciting samples at 3.06 eV with ps-pulsed diode lasers. The emitted light was dispersed with a spectrometer and detected with a charge-coupled device. Transient PL measurements were carried out using ≈70 ps pulses at 3.06 eV from a pulsed diode laser (Picoquant LDH-P series). The emitted light was collected with a phototube coupled to time-correlated single-photon counting unit (time resolution ≈ 600 ps). Temperature-dependent PL and time-resolved PL measurements were carried out on NC thin films drop-casted on quartz substrates and mounted inside a cryostat with optical access.  $\Phi_{PL}$  measurements were carried out in an integrating sphere by exciting the NCs drop casted on silica with a continuous wave diode laser at 3.1 eV. The emitted light was dispersed with a spectrometer and detected with a charge-coupled device. The same films were mounted in the variable temperature insert of a closed cycle He cryostat for evaluating the evolution of the  $\Phi_{PL}$  with decreasing temperature.

**Transient Transmission Spectroscopy:** For the ultrafast transient transmission measurements, the laser source was a Ti:sapphire laser with chirped pulse amplification (Coherent LIBRA-HE), which provided 95 fs pulses at 800 nm at a repetition rate of 2 kHz. The excitation pulses at 3.1 eV were obtained by second harmonic generation in a 1 mm thick  $\beta$  barium borate crystal. Pump pulse duration ≈ 100 fs. The probe beam was a white light supercontinuum generated by focusing a small fraction of the fundamental beam onto a 2 mm thick sapphire plate. After chopping the pump beam at 1 kHz, pump and probe were focused on the sample by means of a lens and a spherical mirror. Pump fluence on the sample position was ≈ 80  $\mu$ J cm<sup>-2</sup>. A computer-controlled optical multichannel analyzer working at the repetition rate of the laser source acquires the map of the differential transmission  $\Delta T/T = (T_{on} - T_{off})/T_{off}$ , as a function of the pump–probe time delay;  $T_{on}$  and  $T_{off}$  are the probe spectra transmitted by the excited and unperturbed samples.

**MCD Measurements:** MCD measures the normalized difference in transmission between left- and right-circularly polarized light through films of nanocrystals in the Faraday geometry. Nanocrystal films were mounted in the variable-temperature insert (1.5–300 K) of a 7 T superconducting magnet with direct optical access. Probe light of tunable wavelength was derived from a xenon lamp directed through a spectrometer. The probe light was mechanically chopped at 137 Hz and was modulated between right and left circular polarizations at 50 kHz using a photoelastic modulator. The transmitted light was detected with a silicon avalanche photodiode.

**Monte Carlo Ray-Tracing Simulation:** The simulations of the squared LSC with increasing lateral size ( $L = 5$  cm, 10 cm, 20 cm, 50 cm, 1 m and 2 m) are performed via a Monte Carlo ray-tracing method, in which



the photon propagation follows the geometrical optics laws. Because the LSC thickness (0.5 cm) is much larger than the light coherence length, interference has been neglected. The stochastic nature of the simulations is reflected in the fact that the ray is transmitted or reflected with the probabilities proportional to respective energy fluxes given by Fresnel Laws. The dependence of these probabilities on the state of polarization of the incident ray (e.g., s- or p-polarized) is also considered. A specific event (i.e., transmission or reflection) is chosen according to random Monte Carlo drawing. Monte Carlo ray-tracing simulations of the LSC were performed using the experimental absorption spectra of the NCs in solution and their relative photoluminescence spectra. AM 1.5G Solar spectrum is employed as LSC excitation source. Once a photon is absorbed by a NC, the subsequent fate of the excitation (i.e., reemission or nonradiative relaxation) is again determined by the Monte Carlo sampling according to the emission quantum yield, set as equal for all the samples ( $\Phi_{\text{PL}} = 95\%$ ). The direction of reemission is distributed uniformly, and the reemission wavelength is determined using the rejection sampling applied to the accurate NCs PL spectra obtained from experiment. The ultimate fate of each photon is either loss due to nonradiative recombination or escape from the LSC via one of the interfaces. A single-ray Monte Carlo simulation is typically repeated  $10^6$ – $10^7$  times to have a proper statistical averaging. A stochastic nature of simulations allows one to easily evaluate LSCs performance, such as the optical quantum efficiency (edge-emitted photons per absorbed solar photons) and the optical efficiency (edge-emitted photons per impinging solar photons).

**Fabrication of the Nanocomposite Luminescent Solar Concentrators:** The PMMA waveguide was fabricated by bulk polymerization using the industrial cell-casting process. The process was characterized by two steps. First, the so-called “syrup” was prepared: the monomer, purified through a basic aluminum oxide column, was heated in a beaker to 80 °C. When the MMA temperature stabilized, AIBN (100 ppm w/w with respect to MMA) was added. At that point, the prepolymerization (an exothermic process) took place and the monomer temperature increased up to the MMA boiling temperature (95 °C); when the monomer achieved the stage of vigorous boiling the syrup was quenched. In the second step, the prepolymer was degassed by four freeze–pump–thaw cycles in order to remove oxygen and introduce argon atmosphere and then mixed with the dispersion of the QDs in MMA containing lauryl peroxide (400 ppm w/w with respect to MMA) described above (10% w/w with respect to the syrup). Finally, the viscous liquid was introduced into the casting mold under argon flow where the polymerization reaction proceeded. Casting mold was made by two glass plates sealed with a polyvinyl chloride (PVC) gasket (in order to preserve the inert atmosphere) and clamped together. The clamps contained springs in order to accommodate the shrinkage of the polymer plate during the polymerization process. Casting mold was placed in a water bath at 55 °C for 48 h. Finally, the slab was post-cured in the oven at 115 °C overnight.

**Characterization of the Polymeric Nanocomposite:** The amount of residual monomer in the PMMA composites was extracted from the  $^1\text{H}$  nuclear magnetic resonance (NMR) spectra, recorded on samples dissolved in deuterated chloroform by using an Avance 500 NMR spectrometer (Bruker). Tetramethylsilane was used as the internal standard. The glass transition temperature of the PMMA matrix was measured by Molecular weights and molecular weight distributions of PMMA matrices were determined by gel permeation chromatography (GPC) using a WATERS 1515 isocratic equipped with a HPLC Pump, WATERS 2414 refractive index detector, four Styragel columns (HR2, HR3, HR4, and HR5 in the effective molecular weight range of 500–20 000, 500–30 000, 50 000–600 000, and 50 000–4000 000 respectively) with tetrahydrofuran (THF) as the eluent at a flow rate of 1.0 mL min $^{-1}$ . The GPC system was calibrated with standard polystyrene from Sigma-Aldrich. GPC samples were prepared by dissolution in THF. The solution was stirred at 80 °C under reflux for 24 h. The QDs were precipitated in THF and removed by centrifugation (6000 rpm for 15 min). The supernatant made of the polymeric matrix dissolved in the eluent was filtered with a hydrophobic PTFE membrane (pore size 0.2  $\mu\text{m}$ ) and measured.

## Supporting Information

Supporting Information is available from the Wiley Online Library or from the author.

## Acknowledgements

A.A. and M.L.Z. contributed equally to this work. A.A., M.L.Z., C.C., V.P., F.M., and S.B. thank the MIUR “Dipartimenti di Eccellenza 2017 Project – Materials for Energy”. Work at the NHMFL was supported by NSF DMR-1644779, the State of Florida, and the US DOE. A.C. and M.Z.-R. acknowledge the project MIUR-PRIN 2015 Grant No. 2015WTW7J3 for financial support. G.G., M.G., C.C., F.B., F.M., and S.B. thank the Provincia Autonoma di Trento for financial support (Nanofarm Project).

## Conflict of Interest

The authors declare no conflict of interest.

## Keywords

CuInS $_2$ , luminescent solar concentrators, Monte Carlo modeling, semiconductor nanocrystals, spectroscopy

Received: August 13, 2019  
Revised: September 28, 2019  
Published online:

- [1] a) S. M. Kobosko, P. V. Kamat, *J. Phys. Chem. C* **2018**, *122*, 14336; b) D. H. Jara, S. J. Yoon, K. G. Stamplecoskie, P. V. Kamat, *Chem. Mater.* **2014**, *26*, 7221; c) V. R. Voggu, J. Sham, S. Pfeffer, J. Pate, L. Phillip, T. B. Harvey, R. M. Brown, B. A. Korgel, *ACS Energy Lett.* **2017**, *2*, 574; d) J. E. Halpert, F. S. F. Morgenstern, B. Ehrler, Y. Vaynzof, D. Credgington, N. C. Greenham, *ACS Nano* **2015**, *9*, 5857; e) I. Levchuk, C. Würth, F. Krause, A. Osvet, M. Batentschuk, U. Resch-Genger, C. Kolbeck, P. Herre, H. P. Steinrück, W. Peukert, C. J. Brabec, *Energy Environ. Sci.* **2016**, *9*, 1083; f) J. Tang, S. Hinds, S. O. Kelley, E. H. Sargent, *Chem. Mater.* **2008**, *20*, 6906.
- [2] a) F. Meinardi, H. McDaniel, F. Carulli, A. Colombo, K. A. Velizhanin, N. S. Makarov, R. Simonutti, V. I. Klimov, S. Brovelli, *Nat. Nanotechnol.* **2015**, *10*, 878; b) K. Wu, H. Li, V. I. Klimov, *Nat. Photonics* **2018**, *12*, 105; c) C. Li, W. Chen, D. Wu, D. Quan, Z. Zhou, J. Hao, J. Qin, Y. Li, Z. He, K. Wang, *Sci. Rep.* **2015**, *5*, 17777; d) M. R. Bergren, N. S. Makarov, K. Ramasamy, A. Jackson, R. Guglielmetti, H. McDaniel, *ACS Energy Lett.* **2018**, *3*, 520.
- [3] a) Z. Bai, W. Ji, D. Han, L. Chen, B. Chen, H. Shen, B. Zou, H. Zhong, *Chem. Mater.* **2016**, *28*, 1085; b) B. Chen, H. Zhong, W. Zhang, Z. a. Tan, Y. Li, C. Yu, T. Zhai, Y. Bando, S. Yang, B. Zou, *Adv. Funct. Mater.* **2012**, *22*, 2081; c) W. Zhang, Q. Lou, W. Ji, J. Zhao, X. Zhong, *Chem. Mater.* **2014**, *26*, 1204; d) D. Aldakov, A. Lefrançois, P. Reiss, *J. Mater. Chem. C* **2013**, *1*, 3756; e) Z. Tan, Y. Zhang, C. Xie, H. Su, J. Liu, C. Zhang, N. Dellas, S. E. Mohney, Y. Wang, J. Wang, J. Xu, *Adv. Mater.* **2011**, *23*, 3553.
- [4] a) J. Kolny-Olesiak, H. Weller, *ACS Appl. Mater. Interfaces* **2013**, *5*, 12221; b) M. G. Panthani, T. A. Khan, D. K. Reid, D. J. Hellebusch, M. R. Rasch, J. A. Maynard, B. A. Korgel, *Nano Lett.* **2013**, *13*, 4294.
- [5] a) Z. Sun, G. Sitbon, T. Pons, A. A. Bakulin, Z. Chen, *Sci. Rep.* **2015**, *5*, 10626; b) H. J. Yun, J. Lim, A. S. Fuhr, N. S. Makarov, S. Keene, M. Law, J. M. Pietryga, V. I. Klimov, *ACS Nano* **2018**, *12*, 12587.

- [6] a) A. Singh, C. Coughlan, D. J. Milliron, K. M. Ryan, *Chem. Mater.* **2015**, *27*, 1517; b) L. De Trizio, M. Prato, A. Genovese, A. Casu, M. Povia, R. Simonutti, M. J. P. Alcocer, C. D'Andrea, F. Tassone, L. Manna, *Chem. Mater.* **2012**, *24*, 2400; c) O. Yarema, D. Bozyigit, I. Rousseau, L. Nowack, M. Yarema, W. Heiss, V. Wood, *Chem. Mater.* **2013**, *25*, 3753; d) J. F. L. Lox, Z. Dang, V. M. Dzhagan, D. Spittel, B. Martín-García, I. Moreels, D. R. T. Zahn, V. Lesnyak, *Chem. Mater.* **2018**, *30*, 2607; e) H. Zhong, S. S. Lo, T. Mirkovic, Y. Li, Y. Ding, Y. Li, G. D. Scholes, *ACS Nano* **2010**, *4*, 5253.
- [7] C. Xia, J. D. Meeldijk, H. C. Gerritsen, C. de Mello Donega, *Chem. Mater.* **2017**, *29*, 4940.
- [8] a) L. Li, A. Pandey, D. J. Werder, B. P. Khanal, J. M. Pietryga, V. I. Klimov, *J. Am. Chem. Soc.* **2011**, *133*, 1176; b) H. Zhong, Z. Bai, B. Zou, *J. Phys. Chem. Lett.* **2012**, *3*, 3167.
- [9] a) X. Hu, R. Kang, Y. Zhang, L. Deng, H. Zhong, B. Zou, L.-J. Shi, *Opt. Express* **2015**, *23*, A858; b) K. E. Knowles, T. B. Kilburn, D. G. Alzate, S. McDowall, D. Gamelin, *Chem. Commun.* **2015**, *51*, 9129.
- [10] F. Meinardi, F. Bruni, S. Brovelli, *Nat. Rev. Mater.* **2017**, *2*, 17072.
- [11] A. C. Berends, M. J. J. Mangnus, C. Xia, F. T. Rabouw, C. de Mello Donega, *J. Phys. Chem. Lett.* **2019**, *10*, 1600.
- [12] A. Shabaev, M. J. Mehl, A. L. Efros, *Phys. Rev. B* **2015**, *92*, 035431.
- [13] a) K. E. Knowles, H. D. Nelson, T. B. Kilburn, D. R. Gamelin, *J. Am. Chem. Soc.* **2015**, *137*, 13138; b) K. E. Hughes, S. R. Ostheller, H. D. Nelson, D. R. Gamelin, *Nano Lett.* **2019**, *19*, 1318.
- [14] V. Pinchetti, Q. Di, M. Lorenzon, A. Camellini, M. Fasoli, M. Zavelani-Rossi, F. Meinardi, J. Zhang, S. A. Crooker, S. Brovelli, *Nat. Nanotechnol.* **2018**, *13*, 145.
- [15] a) A. D. P. Leach, J. E. Macdonald, *J. Phys. Chem. Lett.* **2016**, *7*, 572; b) W. Hu, J. Ludwig, B. Pattengale, S. Yang, C. Liu, X. Zuo, X. Zhang, J. Huang, *J. Phys. Chem. C* **2018**, *122*, 974.
- [16] a) C. Xia, W. Wu, T. Yu, X. Xie, C. van Oversteeg, H. C. Gerritsen, C. de Mello Donega, *ACS Nano* **2018**, *12*, 8350; b) A. C. Berends, F. T. Rabouw, F. C. M. Spoor, E. Bladt, F. C. Grozema, A. J. Houtepen, L. D. A. Siebbeles, C. de Mello Donega, *J. Phys. Chem. Lett.* **2016**, *7*, 3503; c) H. Zang, H. Li, N. S. Makarov, K. A. Velizhanin, K. Wu, Y.-S. Park, V. I. Klimov, *Nano Lett.* **2017**, *17*, 1787.
- [17] a) V. Pinchetti, M. Lorenzon, H. McDaniel, R. Lorenzi, F. Meinardi, V. I. Klimov, S. Brovelli, *Nano Lett.* **2017**, *17*, 4508; b) A. S. Fuhr, H. J. Yun, N. S. Makarov, H. Li, H. McDaniel, V. I. Klimov, *ACS Photonics* **2017**, *4*, 2425; c) W. van der Stam, M. de Graaf, S. Gudjonsdottir, J. J. Geuchies, J. J. Dijkema, N. Kirkwood, W. H. Evers, A. Longo, A. J. Houtepen, *ACS Nano* **2018**, *12*, 11244.
- [18] W. D. Rice, H. McDaniel, V. I. Klimov, S. A. Crooker, *J. Phys. Chem. Lett.* **2014**, *5*, 4105.
- [19] A. Pandey, S. Brovelli, R. Viswanatha, L. Li, J. M. Pietryga, V. I. Klimov, S. A. Crooker, *Nat. Nanotechnol.* **2012**, *7*, 792.
- [20] W. Liu, Y. Zhang, W. Zhai, Y. Wang, T. Zhang, P. Gu, H. Chu, H. Zhang, T. Cui, Y. Wang, J. Zhao, W. W. Yu, *J. Phys. Chem. C* **2013**, *117*, 19288.
- [21] D. W. Houck, E. I. Assaf, H. Shin, R. M. Greene, D. R. Pernik, B. A. Korgel, *J. Phys. Chem. C* **2019**, *123*, 9544.
- [22] I. T. Kraatz, M. Booth, B. J. Whitaker, M. G. D. Nix, K. Critchley, *J. Phys. Chem. C* **2014**, *118*, 24102.
- [23] A. D. P. Leach, X. Shen, A. Faust, M. C. Cleveland, A. D. La Croix, U. Banin, S. T. Pantelides, J. E. Macdonald, *J. Phys. Chem. C* **2016**, *120*, 5207.
- [24] H. D. Nelson, D. R. Gamelin, *J. Phys. Chem. C* **2018**, *122*, 18124.
- [25] G. Nagamine, H. B. Nunciaroni, H. McDaniel, A. L. Efros, C. H. de Brito Cruz, L. A. Padilha, *Nano Lett.* **2018**, *18*, 6353.
- [26] G. K. Grandhi, R. Viswanatha, *J. Phys. Chem. Lett.* **2013**, *4*, 409.
- [27] R. Viswanatha, S. Brovelli, A. Pandey, S. A. Crooker, V. I. Klimov, *Nano Lett.* **2011**, *11*, 4753.
- [28] a) S. A. Crooker, T. Barrick, J. A. Hollingsworth, V. I. Klimov, *Appl. Phys. Lett.* **2003**, *82*, 2793; b) M. Nirmal, D. J. Norris, M. Kuno, M. G. Bawendi, A. L. Efros, M. Rosen, *Phys. Rev. Lett.* **1995**, *75*, 3728.
- [29] a) A. L. Efros, M. Rosen, M. Kuno, M. Nirmal, D. J. Norris, M. Bawendi, *Phys. Rev. B* **1996**, *54*, 4843; b) R. Romestain, G. Fishman, *Phys. Rev. B* **1994**, *49*, 1774.
- [30] M. Booth, A. P. Brown, S. D. Evans, K. Critchley, *Chem. Mater.* **2012**, *24*, 2064.
- [31] R. Xie, M. Rutherford, X. Peng, *J. Am. Chem. Soc.* **2009**, *131*, 5691.
- [32] C. Capitani, V. Pinchetti, G. Gariano, B. Santiago-González, C. Santambrogio, M. Campione, M. Prato, R. Brescia, A. Camellini, F. Bellato, F. Carulli, A. Anand, M. Zavelani-Rossi, F. Meinardi, S. A. Crooker, S. Brovelli, *Nano Lett.* **2019**, *19*, 1307.
- [33] D. A. Bussian, S. A. Crooker, M. Yin, M. Brynda, A. L. Efros, V. I. Klimov, *Nat. Mater.* **2009**, *8*, 35.
- [34] B. K. Ridley, *Quantum Processes in Semiconductors*, Oxford University Press, Oxford **1999**.
- [35] J. H. Blokland, V. I. Claessen, F. J. P. Wijnen, E. Groeneveld, C. de Mello Donega, D. Vanmaekelbergh, A. Meijerink, J. C. Maan, P. C. M. Christianen, *Phys. Rev. B* **2011**, *83*, 035304.
- [36] J. Eilers, J. van Hest, A. Meijerink, C. d. M. Donega, *J. Phys. Chem. C* **2014**, *118*, 23313.
- [37] a) A. Granados del Águila, E. Groeneveld, J. C. Maan, C. de Mello Donega, P. C. M. Christianen, *ACS Nano* **2016**, *10*, 4102; b) S. Brovelli, R. D. Schaller, S. A. Crooker, F. García-Santamaría, Y. Chen, R. Viswanatha, J. A. Hollingsworth, H. Htoon, V. I. Klimov, *Nat. Commun.* **2011**, *2*, 280.
- [38] D. Oron, A. Aharoni, C. de Mello Donega, J. van Rijssel, A. Meijerink, U. Banin, *Phys. Rev. Lett.* **2009**, *102*, 177402.
- [39] C. Robert, T. Amand, F. Cadiz, D. Lagarde, E. Courtade, M. Manca, T. Taniguchi, K. Watanabe, B. Urbaszek, X. Marie, *Phys. Rev. B* **2017**, *96*, 155423.
- [40] M. G. Debije, C. Tzikas, V. A. Rajkumar, M. M. de Jong, *Renewable Energy* **2017**, *113*, 1288.
- [41] N. Aste, L. C. Tagliabue, C. Del Pero, D. Testa, R. Fusco, *Renewable Energy* **2015**, *76*, 330.
- [42] M. G. Debije, *Adv. Funct. Mater.* **2010**, *20*, 1498.
- [43] R. Lesnyuk, V. Lesnyak, A. Herguth, D. Popovych, Y. Bobitski, C. Klinke, N. Gaponik, *J. Mater. Chem. C* **2017**, *5*, 11790.
- [44] M. Uehara, K. Watanabe, Y. Tajiri, H. Nakamura, H. Maeda, *J. Chem. Phys.* **2008**, *129*, 134709.
- [45] F. Meinardi, A. Colombo, K. A. Velizhanin, R. Simonutti, M. Lorenzon, L. Beverina, R. Viswanatha, V. I. Klimov, S. Brovelli, *Nat. Photonics* **2014**, *8*, 392.
- [46] a) F. Meinardi, S. Ehrenberg, L. Dharmo, F. Carulli, M. Mauri, F. Bruni, R. Simonutti, U. Kortshagen, S. Brovelli, *Nat. Photonics* **2017**, *11*, 177; b) F. Meinardi, Q. A. Akkerman, F. Bruni, S. Park, M. Mauri, Z. Dang, L. Manna, S. Brovelli, *ACS Energy Lett.* **2017**, *2*, 2368.
- [47] a) H. Zhong, Y. Zhou, M. Ye, Y. He, J. Ye, C. He, C. Yang, Y. Li, *Chem. Mater.* **2008**, *20*, 6434; b) D.-E. Nam, W.-S. Song, H. Yang, *J. Colloid Interface Sci.* **2011**, *361*, 491.